Composite Structures 225 (2019) 111149

Contents lists available at ScienceDirect

Composite Structures

journal homepage: www.elsevier.com/locate/compstruct

Delamination analysis in bimaterials consisting of shape memory alloy and elastoplastic layers

Saeed Hatefi Ardakani, Hesam Moslemzadeh, Soheil Mohammadi*

High Performance Computing Lab, School of Civil Engineering, College of Engineering, University of Tehran, Tehran, Iran

ARTICLE INFO

Keywords:
Delamination analysis
Interface crack
Bimaterial
Shape memory alloys
Elastoplastic material
Path-dependent J-integral

ABSTRACT

Bimetallic shape memory alloy composites, consisting of an active layer of shape memory alloy and a metallic elastoplastic passive layer, are used for designing the sensors and actuators. Delamination analysis in SMA/elastoplastic bimaterial composites is numerically investigated in this study due to the important effects of interface cracks on failure and load bearing response of such composites. It is known that homogeneous elastoplastic material and shape memory alloy show different path-dependent behaviors for prediction of energy release rate near the crack tip. Therefore, evaluation of J-integral for an interface crack between SMA and elastoplastic layers remains a highly complex issue in fracture analysis of such bimaterials. Presuming small-scale phase transformation and yielding zones, path dependency of J-integral for this composite is investigated for a range of mixed-mode loading conditions, and the elastoplastic material properties including the Young's modulus, hardening slope and yield stress. In addition, the maximum transformation strain within the framework of J_2 plasticity for the elastoplastic material and the thermo-mechanical coupling model of Boyd and Lagoudas for the shape memory alloy are studied. Finally, the influence of mixed-mode loading rates on the crack tip fields is comprehensively assessed.

1. Introduction

Nowadays, the demand for new smart materials is increasing due to their outstanding properties and more importantly, in recovering the original characteristics in extreme conditions. Among them, shape memory alloys (SMAs) show excellent behaviors in the forms of pseudoelasticity and shape memory effect [1]. Pseudoelasticity allows for these materials to recover the deformations from a different stress–-strain path during the mechanical unloading, which results in, for instance, an increased fatigue resistance [2]. In addition, the shape memory effect allows for recovering of permanent deformations in a free force state subject to temperature variations [1,3].

SMAs play a key role in producing advanced composites such as multilayer thin films [4], shape memory alloy fiber-reinforced composites [5–7], self-adaptive/ healing damage controller in smart structures [8,9] and embedded SMA foils in laminates [10,11]. Furthermore, SMA strips can well perform as an active layer in laminated composite materials. For instance, Lagoudas et al. [12] considered the adaptive behavior of SMA as smart actuators with aluminum cores in electro-mechanical devices under the thermal condition.

Defects and cracking in materials constitute a major source of failure. Several novel computational approaches have been developed to numerically model fracture behavior of homogenous materials and bimaterial composites; including the extended finite element method [13–21], the isogeometric analysis (IGA) [22–24], the phase field model [25–27], and the minimum energy approach [28–30].

Menk and Bordas proposed an XFEM approach to numerically introduce crack tip enrichments as a function of the order of crack tip singularity λ and an angular function $\psi(\theta)$ for a cracked anisotropic polycrystalline material [31]. While the extended finite element method has been one of the main computational techniques in dealing with general discontinuity and interface crack problems, the isogeometric analysis, based on Non-Uniform Rational B-spline (NURBS), has proved to be a powerful computational method for delamination analysis of bimaterial composites [23,24] in order to capture the derivatives with higher continuity and to define complex geometries more accurately. For instance, Nguyen et al. presented an isogeometric analysis method based on higher order cohesive elements for modelling delamination in 2D L-shaped bimaterial composites and 3D laminated beams [23].

Moreover, the phase field model has been developed as a suitable approach to various crack propagation problems, covering brittle and ductile fracture, dynamic crack propagation, cohesive fracture, soft-tissue fracture, and interface cracks in bimaterial composites [25–27].

* Corresponding author.
E-mail address: smoham@ut.ac.ir (S. Mohammadi).

https://doi.org/10.1016/j.compstruct.2019.111149
Received 23 January 2019; Received in revised form 27 May 2019; Accepted 11 June 2019
Available online 14 June 2019
0263-8223/

Furthermore, Sutula et al. [28–30] presented the minimum energy approach, based on minimizing the total energy of the system, to predict the angle and onset of crack propagation for stable, unstable and partially stable crack growths. However, there is no report of application of these methods for fracture analysis of SMAs.

Due to defects and failures in SMA-based devices, such as sensors and actuators, investigation of facture behavior of SMAs has become an important issue for researchers in recent years. In addition to the analytical and experimental studies on crack analysis in homogenous SMAs [32–43], several numerical studies have addressed the fracture of homogenous SMAs. For example, the finite element method (FEM) was employed by Stam and van der Giessen [44] to investigate the reversibility of phase transformation on the rate of increase of toughness, while Wang et al. [45] studied the stress induced martensitic transformation in the vicinity of sharp pre-cracked models. Later, Freed and Banks-Sills [46] utilized a cohesive zone model to determine crack growth and its influence on toughening behavior of SMAs. Moreover, Jape et al. [47,48] presented a crack growth model for a pre-cracked SMA subjected to thermal variations and constant mechanical loading and investigated the impact of transformation-induced plasticity on fracture parameters of SMA and the shielding effect of transformation behind the crack tip. More recently, the extended finite element method (XFEM), as an efficient computational method for modeling arbitrary discontinuities, was employed by Hatefi Ardakani et al. [49,50] to study the rate of loading, the direction of crack propagation and the mixed mode crack tip parameters of pseudoelastic SMAs.

So far, many attempts have been made to study the behavior of interface cracks in SMA composite bimaterials. Freed et al. [51] used a cohesive zone model to study the significant transformation toughening behavior for interface cracks in SMA composite bimaterials and to correlate the size of transformation zone with the phase angle. On mode-I crack closure, Jin and Bao [52] described an analytical model to control crack opening by optimal position of SMA fibers. Chi et al. [53] interpreted the ductile interfacial debonding by the phase transformation of SMA fibers in the matrix and suggested a method based on the energy balance analysis. Moreover, the pull-out test in SMA hybrid composites with elliptical holes were carried out by Conte et al. [54] to capture failure mechanisms and to evaluate the overall interfacial strength. More recently, Afshar et al. [55] employed a numerical boundary layer approach to examine the influence of loading rate and material characteristics on an interface crack between SMA and elastic material. They illustrated that the energy release rate of the SMA/elastic bimaterial would remain path-dependent.

Bimetallic shape memory alloy composites, consisting of an active shape memory alloy layer and a passive metallic elastoplastic layer, are used for designing the sensors and actuators [56,57]. Due to the existence of interface cracks, investigation of their failure mechanisms is important. The problem becomes more complex because both the phase transformation and the elastoplastic responses show a path-dependent behavior for the energy release rate near the crack tip [58]. Therefore, this study, as an extension to an earlier work [55], focuses on delamination analysis of SMA/elastoplastic bimaterials, as schematically illustrated in Fig. 1. Variations of fracture parameters, including the path dependent J–integral, are examined by changing the material properties, such as the hardening slope and the Young's modulus. The results are presented in detail and in the form of energy release rate, effective plastic strain and phase transformation contours, as well as the angular distribution of temperature.

2. SMA constitutive model

Shape memory alloys are among the metallic materials, which can fully recover the induced deformation. This behavior is due to the phase transformation from the austenite to the martensite phase during thermomechanical loading and unloading, induced by stress and heating processes, respectively.

The constitutive law for SMA is briefly discussed here [1,59]. Assuming the austenite phase as the reference configuration and the Gibbs free energy as the thermodynamical potential, the constitutive law for SMA is presented. First, an additive decomposition of the total strain ε_{ij}^{total} into an elastic strain ε_{ij}^{e}, a thermo elastic strain ε_{ij}^{th} and an inelastic strain ε_{ij}^{in} is performed:

$$\varepsilon_{ij}^{total} = \varepsilon_{ij}^{e} + \varepsilon_{ij}^{th} + \varepsilon_{ij}^{in} \tag{1}$$

The inelastic strain generally includes both the transformation and the plastic-type deformations. In the present study, however, only the transformation strain ($\varepsilon_{ij}^{t} = \varepsilon_{ij}^{in}$) is considered for the SMA inelastic response.

For defining the thermodynamical framework, the Gibbs energy is considered in the additive form of the free elastic energy and the thermal energy (dummy indices$i$, j, k, l are used based on the Einstein notation) [1]:

$$G_e = -\frac{1}{2\rho}\sigma_{ij}D_{ijkl}\sigma_{kl} - \frac{1}{\rho}\sigma_{ij}[\alpha_{ij}(T-T_0)+\varepsilon_{ij}^{t}] + c\left[(T-T_0) - T\ln\left(\frac{T}{T_0}\right)\right] - S_0T + U_0 + \frac{1}{\rho}g(\xi) \tag{2}$$

where D_{ijkl} is the fourth order elastic compliance tensor, and α_{ij} is the second order effective expansion tensor. Moreover, c, S_0 and U_0 are the effective specific heat, the entropy and the internal energy at the reference state, respectively. The reference state is stress-free ($\sigma_{ij} = 0$) and T_0 is the reference temperature of material ($T = T_0$). The transformation hardening function $g(\xi)$ is chosen in a polynomial form [1], and the effective material properties are defined by a linear summation of austenite and martensite volume fractions (ξ), as follows:

$$D_{ijkl}(\xi) = D_{ijkl}^{A} + \xi(D_{ijkl}^{M} - D_{ijkl}^{A}) \tag{3}$$

$$\alpha_{ij}(\xi) = \alpha_{ij}^{A} + \xi(\alpha_{ij}^{M} - \alpha_{ij}^{A}) \tag{4}$$

$$S_0(\xi) = {S_0}^{A} + \xi({S_0}^{M} - {S_0}^{A}) \tag{5}$$

$$u_0(\xi) = {u_0}^{A} + \xi({u_0}^{M} - {u_0}^{A}) \tag{6}$$

$$c(\xi) = c^{A} + \xi(c^{M} - c^{A}) \tag{7}$$

where the austenite and martensite phases are denoted by A and M superscripts, respectively. ξ is set to 0 and 1 for the austenite and martensite phases, respectively.

Using the Gibbs free energy, the total infinitesimal strain can be found as [1],

$$\varepsilon_{ij} = -\rho\frac{\partial G_e}{\partial \sigma_{ij}} = D_{ijkl}\sigma_{kl} + \alpha_{ij}(T-T_0) + \varepsilon_{ij}^{t} \tag{8}$$

Changes in the martensite volume fraction may lead to different material responses. Accordingly, a relation must be defined to compute the evolution of transformation strain from the martensite volume fraction:

$$\dot{\varepsilon}_{ij}^{t} = \Lambda_{ij}\dot{\xi} \tag{9}$$

where Λ_{ij} shows the transformation strain direction, defined for both forward and reverse transformations as,

$$\Lambda_{ij} = \begin{cases} \sqrt{\frac{3}{2}}\varepsilon_{max}^{t}\frac{\sigma_{ij}-\frac{1}{3}\sigma_{ii}}{\sqrt{\sigma_{ij}\sigma_{ij}}}\dot{\xi} > 0 \\ \sqrt{\frac{3}{2}}\varepsilon_{max}^{t}\frac{\varepsilon_{ij}^{t-r}}{\sqrt{\varepsilon_{ij}^{t-r}\varepsilon_{ij}^{t-r}}}\dot{\xi} < 0 \end{cases} \tag{10}$$

ε_{max}^{t}denotes the maximum transformation strain. In addition, ε_{ij}^{t-r} is the transformation strain at the reverse point. For a forward procedure, the transformation surface Θ can be defined by the general thermodynamic force conjugate of the martensite volume fraction [1],

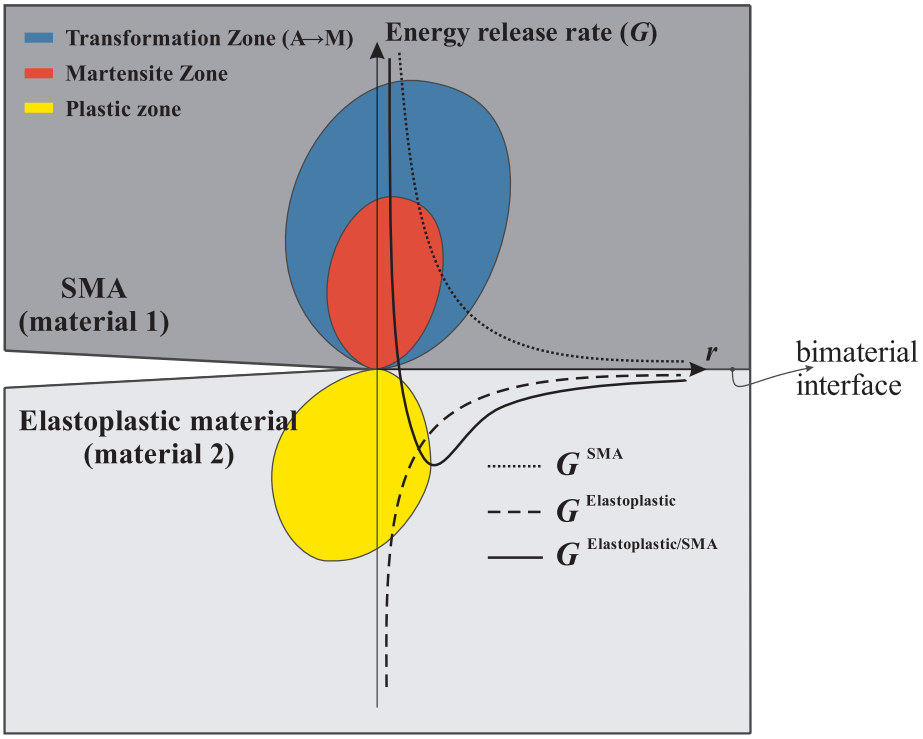

Fig. 1. Schematic representation of the SMA/elastoplastic bimaterial.

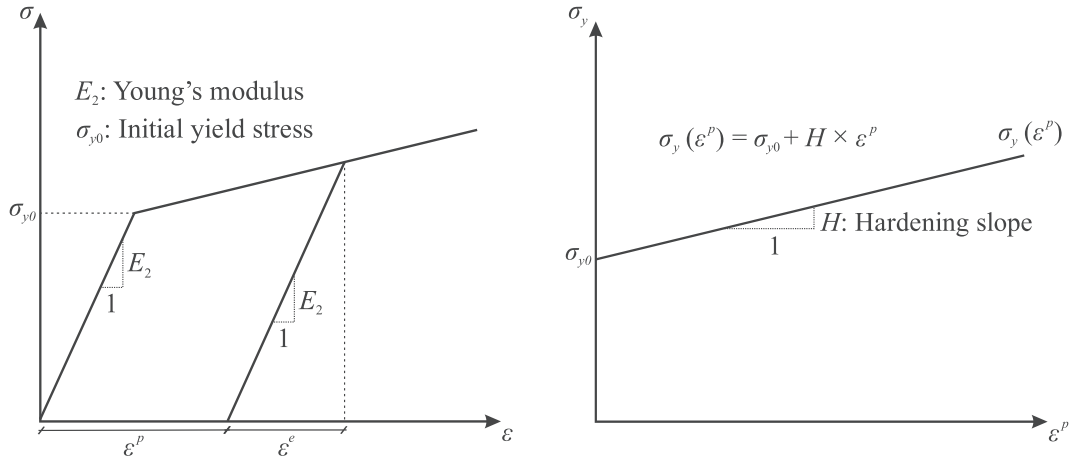

Fig. 2. Typical one-dimensional elastoplastic response.

$$\Theta = \sigma_{ij}\Lambda_{ij} + \frac{1}{2}\sigma_{ij}\Delta D_{ijkl}\sigma_{kl} + \sigma_{ij}\Delta\alpha_{ij}(T - T_0) - \rho\Delta c\left[(T - T_0) - T ln\left(\frac{T}{T_0}\right)\right] + \rho\Delta S_0 T - \rho\Delta U_0 - \frac{\partial g}{\partial \xi} - \frac{1}{4}\rho S_0(T_s^M + T_f^M - T_s^A - T_f^A) \quad (11)$$

where s and f subscripts denote the starting and finishing temperatures, respectively. The forward transformation takes place when:

$$\Theta = 0 \quad (12)$$

3. Elastoplastic constitutive model

The elastoplastic layer is assumed to follow the von Mises yield criterion, and its nonlinear responses in the processes of overloading and unloading are studied [60].

The total strain in an elastoplastic analysis can be written in terms of the elastic strain ε_{ij}^e, the plastic strain ε_{ij}^p and the thermal effects ε_{ij}^{th} (see Fig. 2):

$$\varepsilon_{ij} = \varepsilon_{ij}^e + \varepsilon_{ij}^p + \varepsilon_{ij}^{th} \quad (13)$$

and the corresponding stress can be calculated by:

$$\sigma_{ij} = E_{ijkl}\varepsilon_{kl}^e = E_{ijkl}(\varepsilon_{kl} - \varepsilon_{kl}^p - \varepsilon_{kl}^{th}) \quad (14)$$

where E_{ijkl} is the Young's modulus of the elastoplastic material (E_2 for material 2). The von Mises yield criterion is utilized to control the yielding state in terms of the von Mises equivalent stress σ_e,

$$\sigma_e = \frac{1}{\sqrt{2}}\sqrt{(\sigma_1 - \sigma_2)^2 + (\sigma_2 - \sigma_3)^2 + (\sigma_3 - \sigma_1)^2} \quad (15)$$

The yielding function f_y is then defined as

$$f_y = \sigma_e - \sigma_y = \sqrt{\frac{2}{3}\sigma_{ij}^{dev}\sigma_{ij}^{dev}} - \sigma_y \quad (16)$$

where $\sigma_{ij}^{dev} = \sigma_{ij} - \frac{1}{3}\sigma_{ii}$ represents the deviatoric stress tensor. The

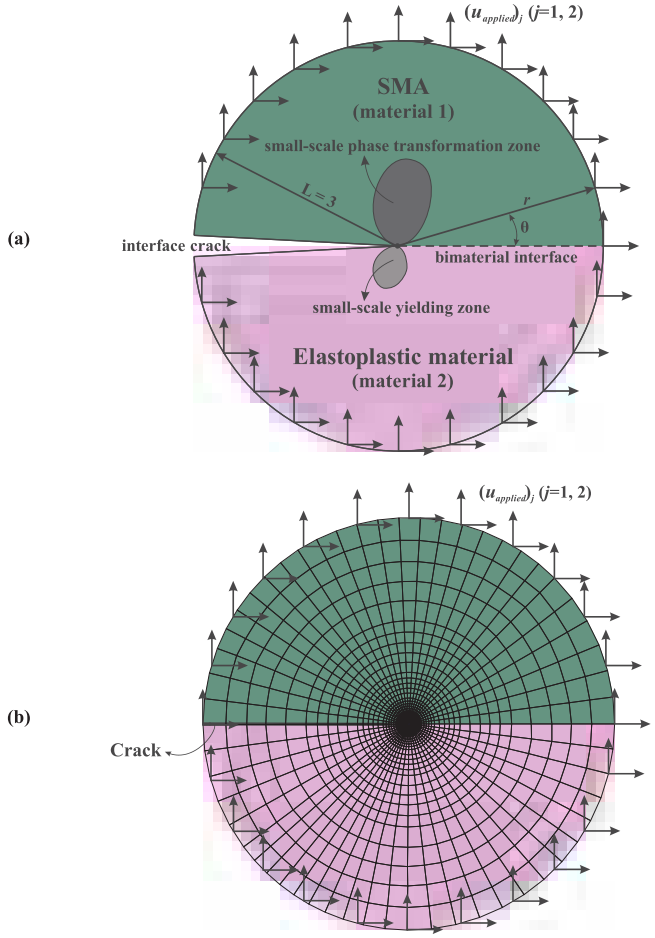

Fig. 3. Boundary layer model (a) K-dominant region, (b) finite element mesh.

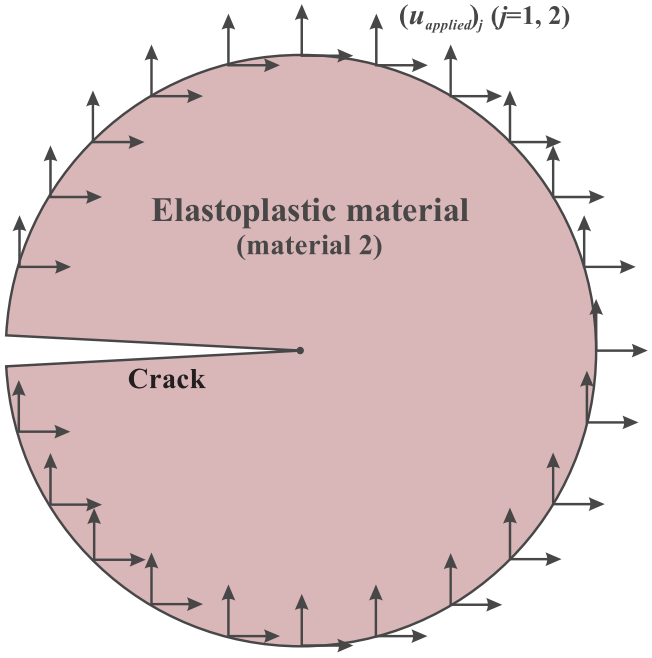

Fig. 4. A homogenous perfect plastic problem.

Table 1
Elastoplastic material properties.

Material parameters	Values
E_2 (GPa)	70
υ_2	0.30
H (GPa)	0
σ_y (MPa)	243

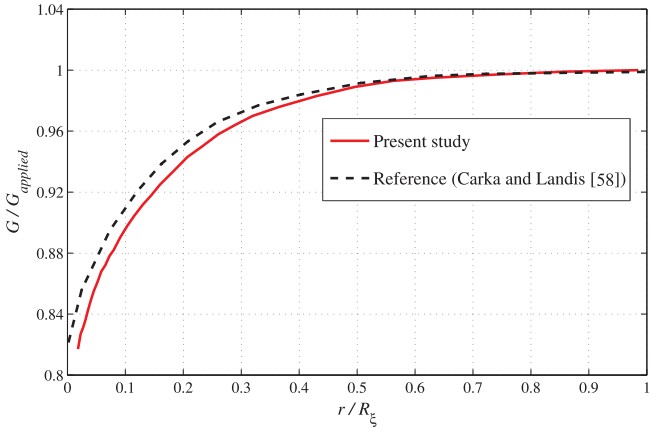

Fig. 5. Variations of normalized energy release rate for the fully perfect plastic problem in the case of crack mode I.

yielding criterion can be described as:

$$\begin{cases} f_y < 0: \textit{Elasticdeformation} \\ f_y \geq 0: \textit{Plasticdeormation} \end{cases} \tag{17}$$

4. Thermo-mechanical coupling effects

The heat equation should fully be coupled with the mechanical equation to take into account the thermomechanical coupling effects [49,61]:

$$\textit{Mechanical equation}: \sigma_{ij,j} + f_i = 0 \tag{18}$$

$$\textit{Heat equation}: T\alpha_{ij}\dot{\sigma}_{ij} + \rho c\dot{T} - \left(\sigma_{ij}\Lambda_{ij} + \frac{1}{2}\sigma_{ij}\Delta D_{ijkl}\sigma_{kl} + \sigma_{ij}\Delta\alpha_{ij}\right.$$
$$\left.(T - T_0) - \rho\Delta c\left[(T - T_0) - Tln\left(\frac{T}{T_0}\right)\right] - \rho\Delta U_0 - \frac{\partial g}{\partial \xi}\right)\dot{\xi} = -Q_{i,i} \tag{19}$$

where the heat flow Q_i is defined as

$$Q_i = -kT_{,i} \tag{20}$$

and k is the thermal conductivity. These coupled equations are iteratively solved by the Newton-Raphson method, as described in detail in [49,61]. It should be noted that no thermo-mechanical coupling is considered for elastoplastic deformations, and Eq. (19) is simplified to $\rho c\dot{T} = (kT_{,i})_{,i}$ for this layer.

5. Fracture mechanics of bimaterial cracks

Existance of a bimaterial interface crack has always been a challenge for engineers studying layered bimaterial problems. The key fracture mechanics parameter for these problems is to evaluate the stress intensity factor K. The complex form of K for bimaterial problems is defined as [62]:

$$K = K_I + iK_{II} = \sqrt{2\pi}\, r^{-i\varepsilon}(\sigma_{22} + i\sigma_{12})_{\theta=0} \tag{21}$$

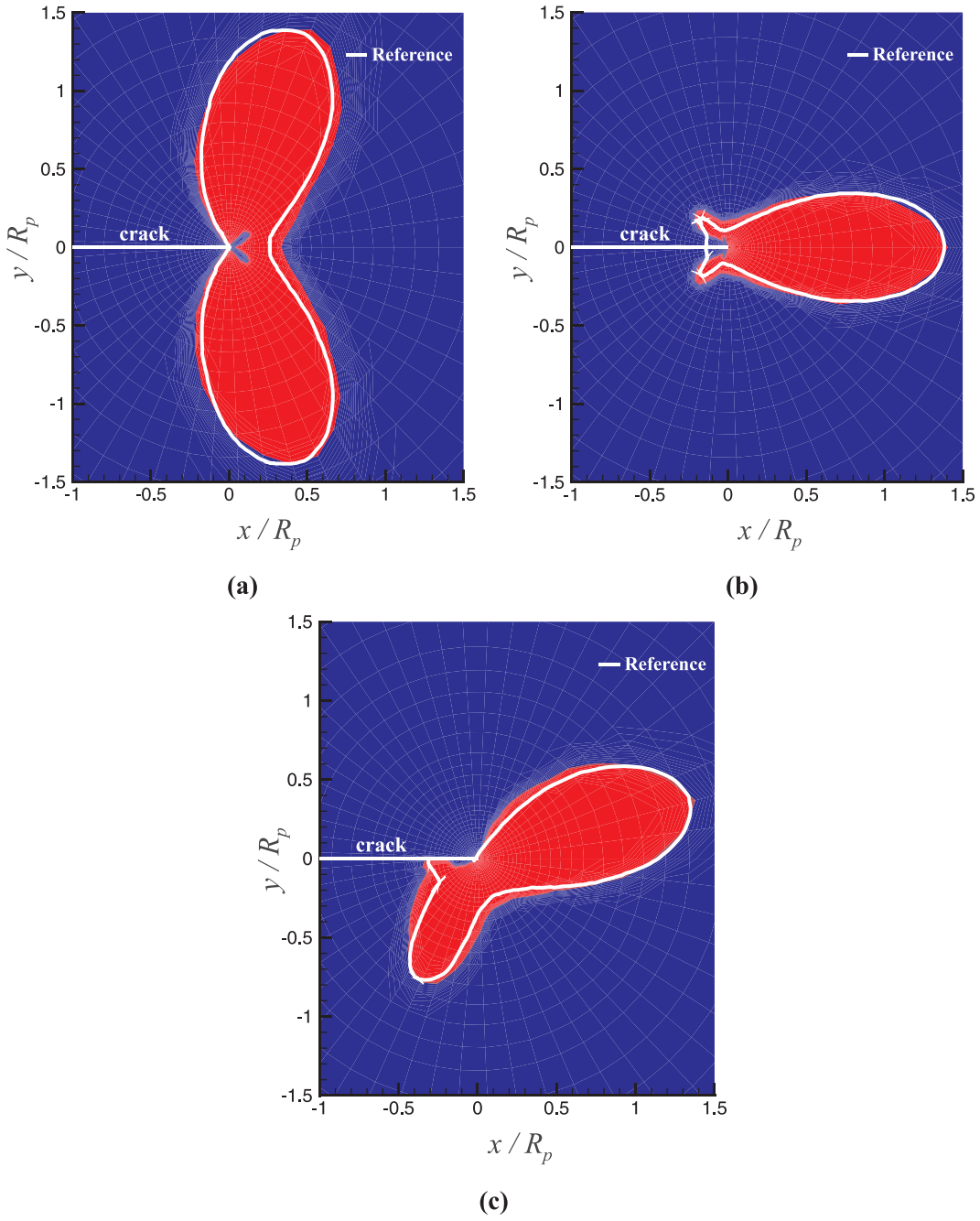

Fig. 6. Plastic zone shapes for three different crack modes (a) mode I, (b) mode II, and (c) mixed mode $K_I = K_{II}$

Table 2
SMA properties.

Material parameters	Values	Material parameters	Values
E_A (GPa)	47	T_s^A (°C)	12
E_M (GPa)	24	T_f^A (°C)	26
υ_A	0.33	C_A (MPa °C^{-1})	8.4
υ_M	0.33	C_M (MPa °C^{-1})	6.7
ε^t_{max}	0.05	c (J.kg^{-1}.K^{-1})	837
T_0 (°C)	35	k (W.m^{-1}. K^{-1})	18.3
T_f^M (°C)	−29	ρ (kg.m^{-3})	6500
T_s^M (°C)	3		

where the bimaterial constant ε is calculated in terms of the second Dunder's parameter β [62]

$$\varepsilon = \frac{1}{2\pi}\ln\left(\frac{1-\beta}{1+\beta}\right) \tag{22}$$

with

$$\beta = \frac{1}{2}\frac{E_2^*\frac{1-2\nu_1}{1-\nu_1} - E_1^*\frac{1-2\nu_2}{1-\nu_2}}{E_1^* + E_2^*} \tag{23}$$

where E_i^* for the plane strain condition is defined as

$$E_i^* = \frac{E_i}{1-\nu_i^2},\ i = 1, 2 \tag{24}$$

where E_i and ν_i are the Young's modulus and the Poison's ratio, respectively. The phase angle Ψ is adopted to quantify the mode-mixity of

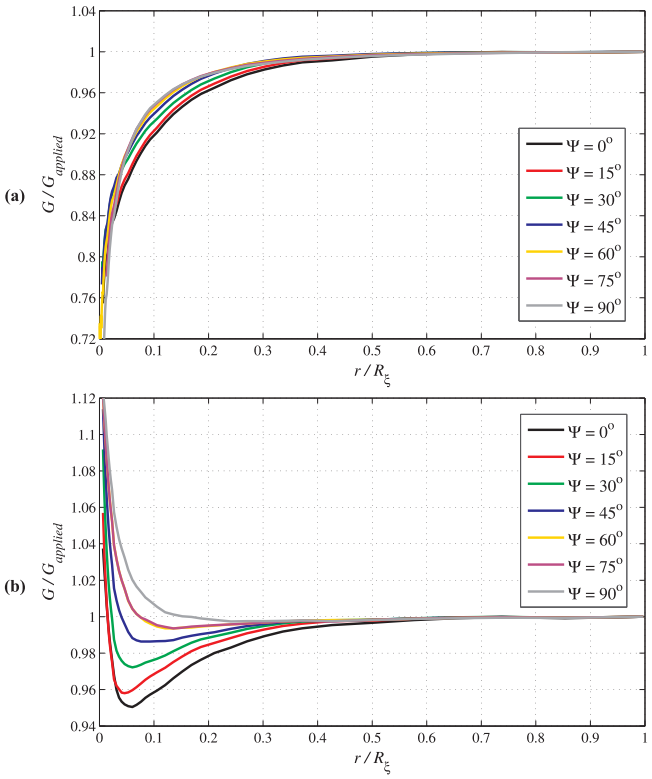

Fig. 7. Effect of mode mixity on the energy release rate near the crack tip (a) $H = 0$, (b) $H = 10$ GPa

the crack tip

$$\Psi = \tan^{-1}\left(\frac{K_2}{K_1}\right) \tag{25}$$

To evaluate the energy release rate, G, which can be used for nonlinear fracture problems, a contour integral (J-integral) approach is adopted:

$$G = J = \int_{\Gamma} (n_i \sigma_{ij} u_{j,1} - W n_1) ds \tag{26}$$

where the strain energy W is defined as

$$W = \int_0^{\varepsilon} \sigma_{ij} d\varepsilon_{ij} \tag{27}$$

and Γ is a crack-closed contour with the normal vector n_i. The equivalent domain integral (EDI) form of (25) can be written as [14,49]:

$$G = J = \int_A (q_{,i} \sigma_{ij} u_{j,1} - W q_{,1} + \alpha \sigma_{ii} T_{,1} q) dA - \int_A (f_i u_{i,1} q) dA - \int_{C^+ + C^-} (t_i u_{i,1} q) dc \tag{28}$$

where q is an arbitrary smooth function with 0 and 1 values on outer and inner boundaries of the domain, respectively.

In this study, t_i and f_i are set to zero, since the problem is assumed with traction-free crack and no body forces f_i.

Despite the fact that the J-integral was originally introduced for linear elastic materials, this technique has been frequently used for fracture analysis in elastoplastic materials [58] and SMAs [49,55,63]. While linear and nonlinear elastic materials, as non-dissipative materials, ensure a path-independent J–integral near the crack tip, it becomes contour dependent in dissipative mechanisms, such as elastoplastic materials and SMAs.

6. Boundary layer approach

The boundary layer approach is adopted to investigate the displacement fields around the crack tip for the plane strain cracked SMA/elastoplastic bimaterial problem (see Fig. 3a). Mixed mode crack tip fields are generated by displacement control boundary conditions on the K-dominant region, which is considered 100 times larger than the phase transformation zone to ensure the assumptions of small-scale phase transformation and yielding zones. Accordingly, the displacement of the region can be defined by the asymptotic expansion

$$(u_{applied})_j = \frac{1+\nu_1}{E_1}\sqrt{\frac{r}{2\pi}}\{\mathrm{Re}[K_{applied}\, r^{i\varepsilon}]\tilde{u}_j^{\mathrm{I}}(\theta, \varepsilon, \nu_1) + \mathrm{Im}[K_{applied}\, r^{i\varepsilon}]\tilde{u}_j^{\mathrm{II}}(\theta, \varepsilon, \nu_1)\} \; (j = 1, 2) \tag{29}$$

where

$$K_{applied} = (K_I)_{applied} + i(K_{II})_{applied} \tag{30}$$

More details on $\tilde{u}_j^{\mathrm{I}}$ and $\tilde{u}_j^{\mathrm{II}}$ can be found in [55]. The corresponding applied energy release rate $G_{applied}$ is defined by

$$G_{applied} = \frac{1}{\bar{E}} \frac{|K_{applied}|^2}{\cosh^2(\pi\varepsilon)} \tag{31}$$

where

$$\frac{2}{\bar{E}} = \frac{1}{E_1^*} + \frac{1}{E_2^*} \tag{32}$$

Numerical predictions of energy release rate near the crack tip will be normalized by $G_{applied}$ in section 7.

Considering a crack located along the interface, with the center of coordinate system located at the crack tip, a radial finite element mesh (5289 four-noded elements) is used to model the problem (see Fig. 3b).

7. Results and discussions

In this section, a mixed mode interface crack in a thermomechanical SMA/elastoplastic bimaterial problem is studied to investigate the phase transformation, temperature distribution and energy release rate. At first, homogenous cracked models are verified for both homogenous SMA and elastoplastic materials. Afterwards, simulations for a plane strain SMA/elastoplastic bimaterial problem is conducted to investigate the interface crack tip parameters in the isothermal condition. Finally, the thermomechanical coupling effects on fracture parameters are comprehensively studied.

7.1. Fully plastic problem

Homogenous SMA problems have been thoroughly examined in previous work [49]. For the case of fully plastic problem, a homogenous perfect plastic problem (see Fig. 4) with material properties of Table 1 is considered and the results are compared with reference [58].

Normalized fracture energy (in terms of the J-value) for different J-integral radii is displayed in Fig. 5. It is observed that the results are consistent with the reference report [58].

Moreover, Fig. 6 illustrates the plastic zone shape for three different crack modes (pure modes I and II, and the mixed mode $K_I = K_{II}$). Clearly, the shape and size of the plastic zone is identical with that of the plastic zone reported in reference [58].

7.2. An interface crack in an SMA/elastoplastic composite in isothermal conditions

Geometry and boundary conditions of the bimaterial composite are assumed to be similar to Fig. 3. It consists of an SMA upper layer (material 1) and an elastoplastic lower material (material 2). The

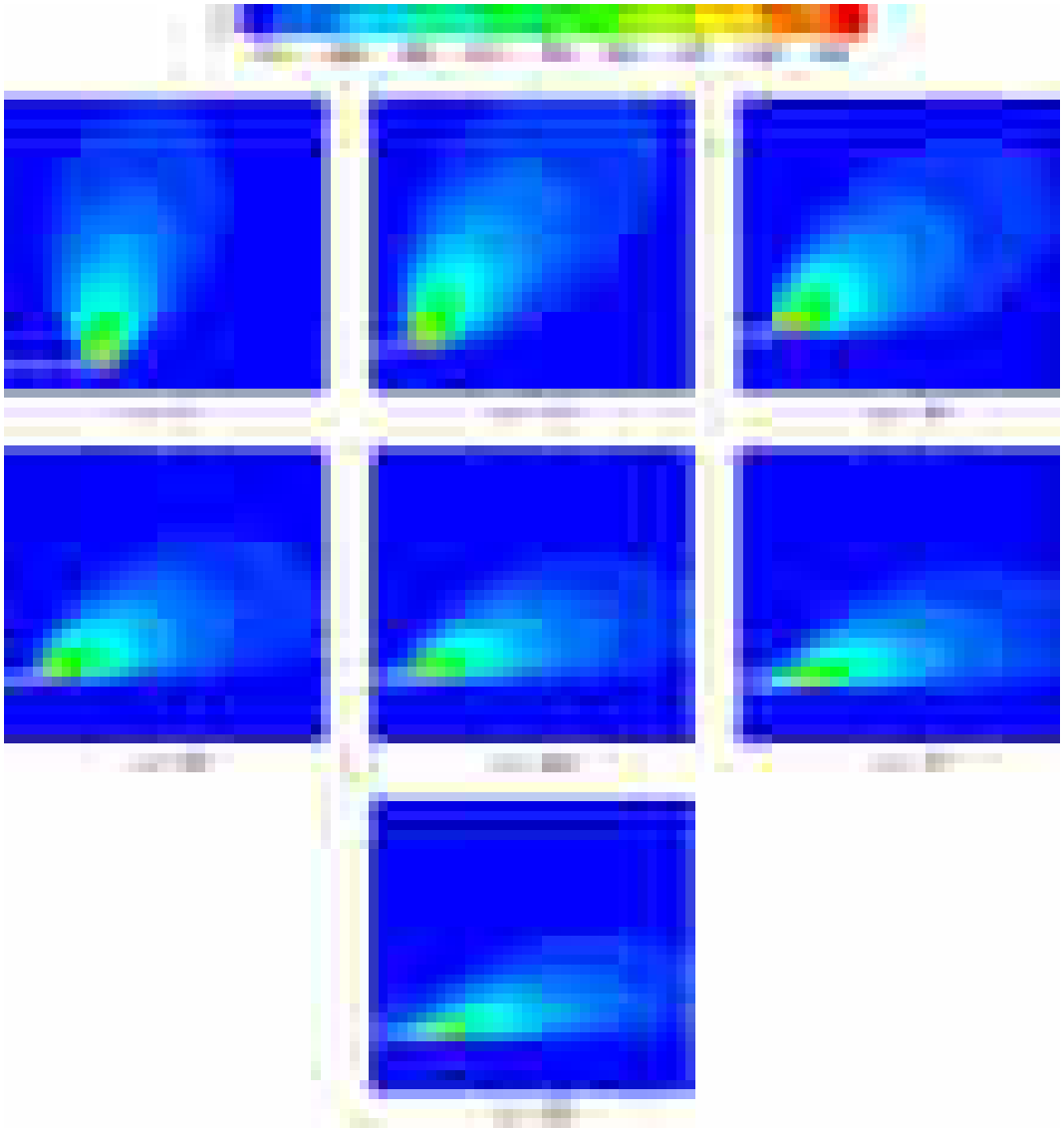

Fig. 8. Distribution of phase transformation around the crack tip for different phase angles

mechanical properties of the upper layer (SMA) and lower layer (elastoplastic material) are presented in Tables 2 and 1, respectively. Considering small-scale phase transformation and yielding zones, a plane strain finite element analysis is performed.

It should be mentioned that for each phase angle, K_I and K_{II} are selected in a way that leads to the same value of $R_\xi = 0.03$. Then, the applied energy release rate $G_{applied}$ is determined from the values of K_I and K_{II} by Eq. (31).

For each phase angle, which specifies the mixed mode condition, the energy release rate is calculated. The results are depicted in Fig. 7 for two cases of hardening slope ($H = 0$ and $H = 10$ GPa). The maximum and minimum values are related to phase angles $\Psi = 0°$ and $\Psi = 90°$, respectively. In regions far from the transformation field, the J-integral has the same value as the applied energy release rate ($G_{applied}$). It is evident from the results that the perfect plastic case ($H = 0$) is not influenced by the phase angle changes. In contrast, for $H = 10$ GPa, the phase angle has a great effect on the results in such a way that even the trend of variations of energy release rate differs for different phase angles. Furthermore, it is observed that the normalized energy release rate experiences values more than one for the case of $H = 10$ GPa, whereas the perfect plastic case is limited to the unity.

According to Figs. 8 and 9, contours of phase transformation and effective plastic strain are presented for seven different phase angles. Clearly, the phase transformation occurs in the upper layer and the plastic deformation is limited to the lower layer. Moreover, it can be observed that the mode mixity has a major effect on the shapes of phase transformation and effective plastic strain zones.

In order to examine the mesh independency of the results, five different finite element meshes (1415, 3293, 5289, 8834, and 12,209 elements) are utilized to solve the problem of SMA/elastoplastic composite with an interface crack in the mixed mode condition $\Psi = 0°$. The energy release rate at two different distances near the crack tip ($r/R_\xi = 0.05, 0.1$) is calculated. Fig. 10 illustrates the error of $G/G_{applied}$ (defined in Eq. (33)) at the mentioned distances. Clearly, a converged solution is obtained for the energy release rate as the mesh is refined.

$$\text{Error} = \frac{G/G_{applied} - G/G_{applied,\ (finest\ mesh)}}{G/G_{applied,\ (finest\ mesh)}} \times 100 \tag{33}$$

Moreover, the sensitivity of the solution near a crack tip is examined by comparing the austenitic and the martensitic boundaries around the crack tip for three fine meshes (5289, 8834, and 12,209 elements). It is clearly observed from Fig. 11 that the austenitic and martensitic boundaries ($\xi = 0$ and $\xi = 1$, respectively) remain the same for all three meshes; an indication of mesh insensitivity and good convergence of

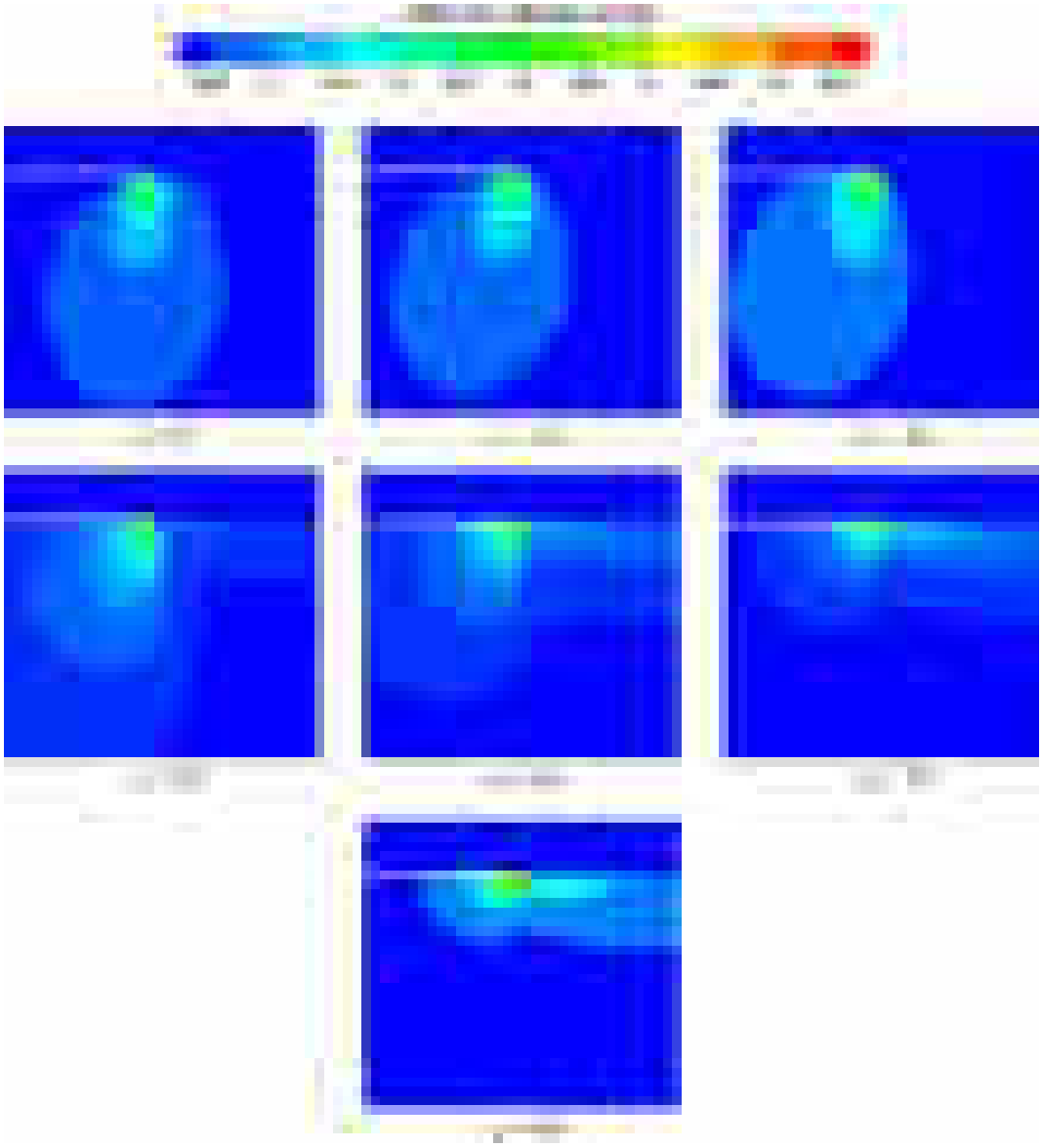

Fig. 9. Distribution of effective plastic strain around the crack tip for different phase angles

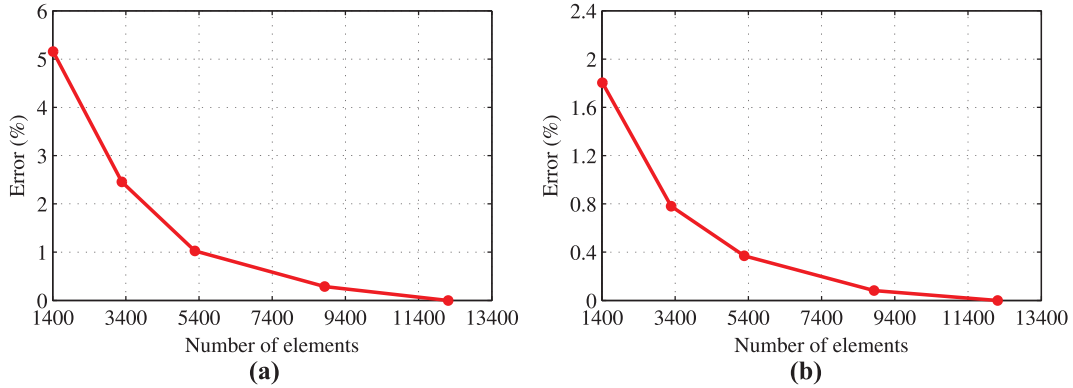

Fig. 10. Error of $G/G_{applied}$ versus five different meshes at two different distances near the crack tip, a) $r/R_{\xi} = 0.05$ and b) $r/R_{\xi} = 0.1$.

the local crack tip solution.

Now, the properties of SMA material is kept constant while the properties of lower material (elastoplastic material) are changed for each simulation. First, the effect of hardening slope (H) on energy release rate is discussed, as depicted in Fig. 12. It is apparent that when the lower material is perfect plastic, plasticity plays a key factor in the values of energy release rate, and as a result, the trend of response tends to become similar a homogenous cracked elastoplastic material.

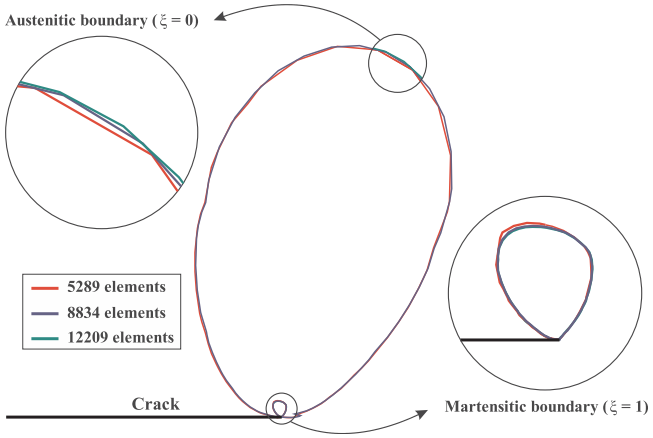

Fig. 11. Austenitic and martensitic boundaries around the crack tip for three fine meshes

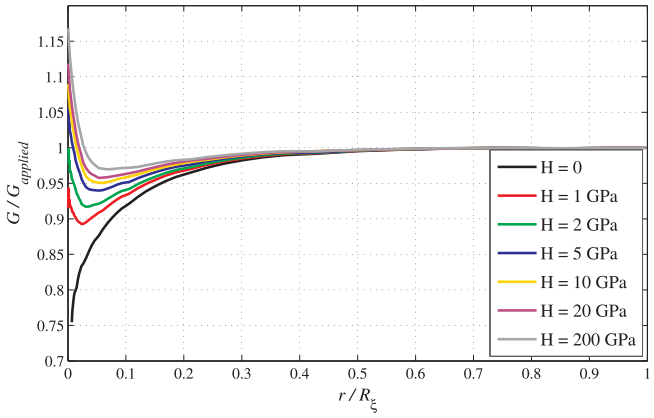

Fig. 12. Effect of hardening slope on the energy release rate

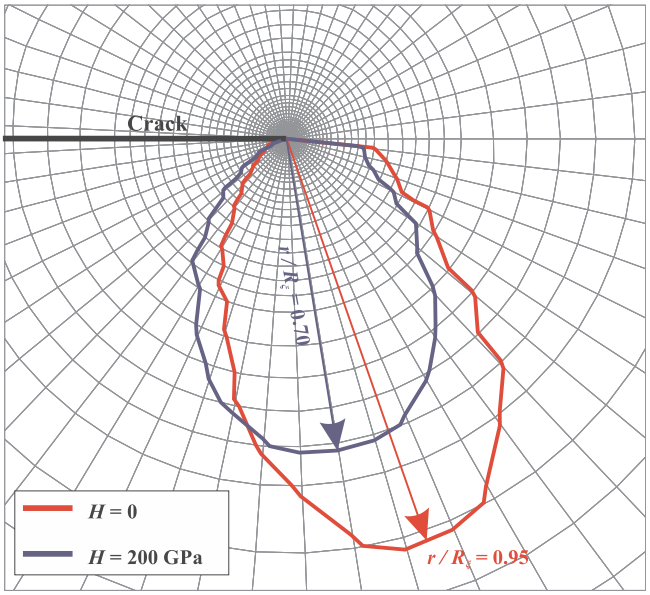

Fig. 13. Plastic zone for two values of H

By increasing H, the trend of results for the SMA/elastoplastic composite becomes noticeably similar to homogenous cracked SMA material. In other words, plasticity loses its effect with larger values of H because they generate smaller plastic strain zones in the vicinity of crack tip, resulting in the reduction of energy release rate. This is better

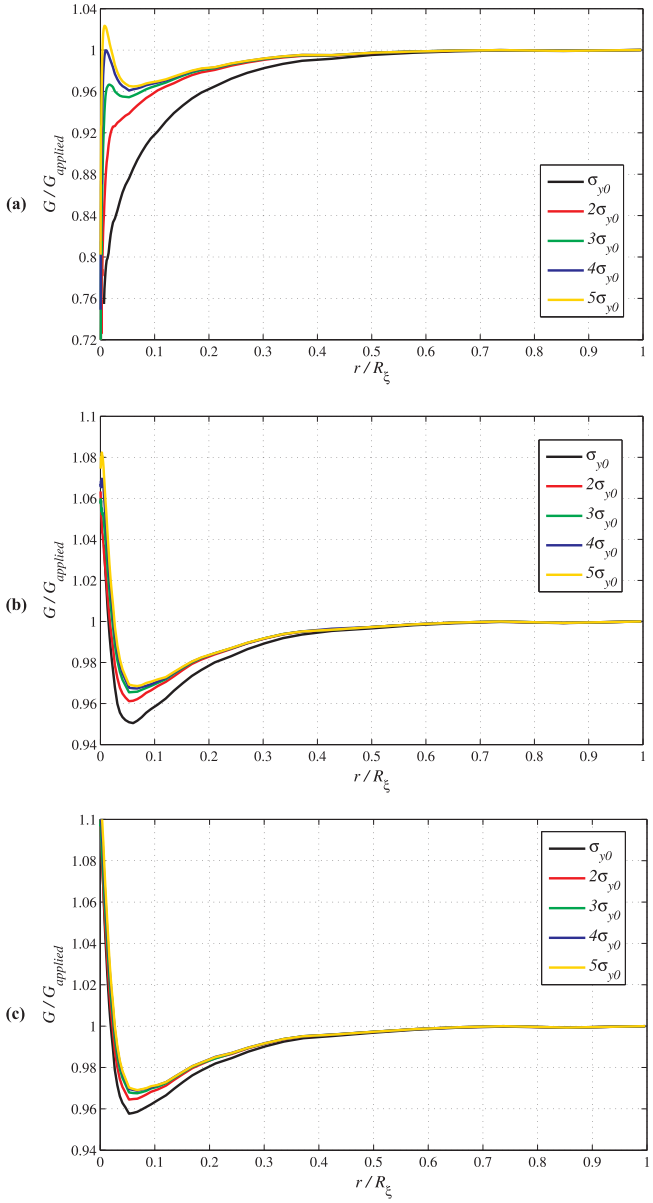

Fig. 14. Effect of initial yield stress on the energy release rate for three hardening slopes (a) $H = 0$, (b) $H = 10$ GPa and (c) $H = 20$ GPa

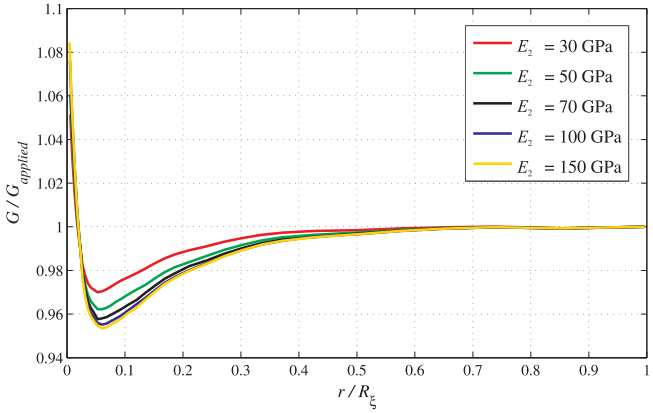

Fig. 15. Effect of E_2on the energy release rate for $H = 20$ GPa

observed in Fig. 13 which illustrates the size of plastic zone for two maximum and minimum values of H ($H = 0$ and $H = 200$ GPa).

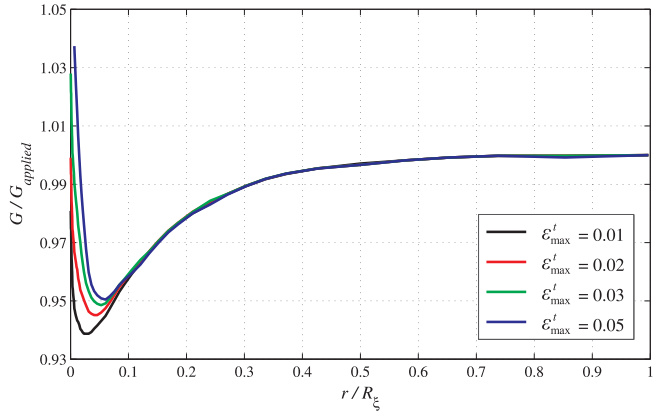

Fig. 16. Effect of maximum transformation strain on the energy release rate for a hardening slope equal to 10 GPa

Table 3
Applied loading rates.

$\dot{G}_{applied}\left(\frac{N}{mm.s}\right)$	Ψ = 0°	Ψ = 15°	Ψ = 30°	Ψ = 45°	Ψ = 60°	Ψ = 90°
Loading rate A	0.248	0.284	0.179	0.152	0.148	0.187
Loading rate B	2.48	2.84	1.79	1.52	1.48	1.87
Loading rate C	24.8	28.4	17.9	15.2	14.8	18.7

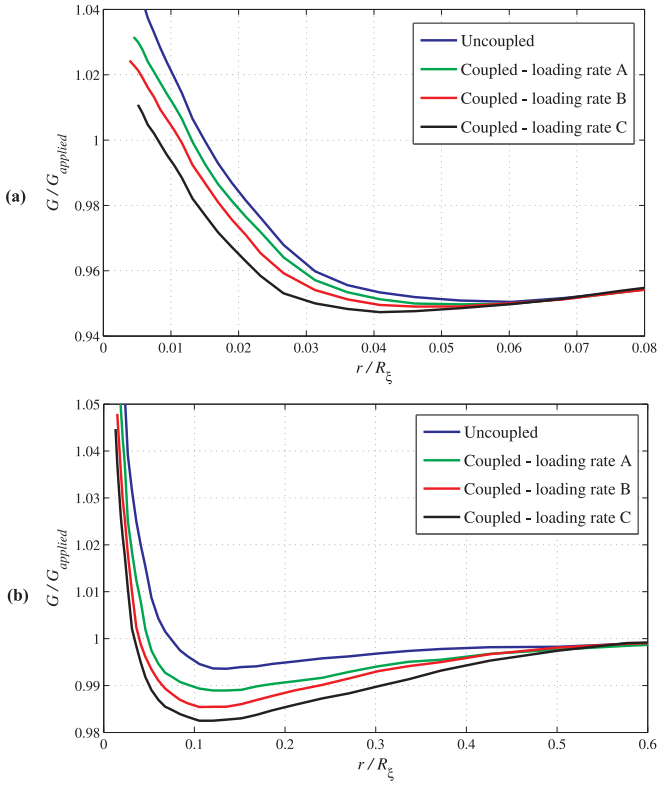

Fig. 17. The effect of applied loading rate on the J-integral near the crack tip for the elastoplastic material with H = 10 GPa, (a) Ψ = 0° , (b) Ψ = 60°

Increase of H from 0 to 200 GPa results in 26% decrease of the radius of plastic zone, indicating the lower effect of plasticity.

For three different values of H (0, 10 GPa, and 20 GPa), the influence of initial yield stress on the fracture behavior of composite is presented in Fig. 14. It is important to point out that with the increase of initial yield stress, the size of plastic region becomes smaller, and consequently, the trend of response becomes more closer to a crack in fully SMA model than a crack in fully elastoplastic model. Furthermore, it is worth to mention that as the value of H increases, the sensitivity of the results to the variations of initial yield stress becomes less significant.

Now, the effect of Young's modulus of elastoplastic material (E_2) on the energy release rate distribution near the crack tip is studied for a specific hardening slope. According to Fig. 15, it can be concluded that the increase of E_2 has no significant effect on the distribution of energy release rate for distances very close to the crack tip. However, at a specific distance of about $r/R_\xi = 0.025$ from the crack tip, a considerable difference between the results starts to appear and continues up to $r/R_\xi = 0.6$, where the effect of E_2 on the energy release rate is lost.

The effect of maximum transformation strain ($\varepsilon^t_{\max}$), as an important parameter of SMA, on the energy release rate is investigated in Fig. 16. It is observed that the effect of maximum transformation strain becomes insignificant at distances greater than $r/R_\xi = 0.1$.

7.3. Thermomechanical coupling conditions

Now, the same SMA/elastoplastic composite simulated in the previous section is used to investigate the thermomechanical coupling effects on the crack tip fields. The thermal boundary condition is applied on the perimeter of the circle in the form of prescribed ambient temperature.

Thermomechanical coupling effects in the forward phase transformation of SMAs produce some latent heat which cannot be ignored in the study of an existing crack. The magnitude of loading rate and the applied time span are among the most important parameters in the analysis of crack tip fields. It is well known that increasing the rate of loading generates more heat around the crack tip [49,55]. To study these noticeable effects, different simulations are now carried out by changing the loading rates, defined as the ratio of applied energy release rate to the total loading time ($\dot{G}_{applied} = G_{applied}$/total loading time). For each mode mixity, three ratios are assumed, as presented in Table 3. Low, medium and high stain rates are termed as the loading rates A, B and C, respectively.

The thermomechanical coupled equations (18) and (19) are numerically solved. The results of the energy release rate, illustrated in Fig. 17, reveal that the generated latent heat in the crack tip induces a reduction in the energy release rate of coupled simulations. In addition, the specific distance [49,55], where the coupling effect is remarkable, differs for the two phase angles Ψ = 0° and Ψ = 60°. In other words, the curves associated to Ψ = 0° converge at $r/R_\xi = 0.06$, while the convergence is achieved at $r/R_\xi = 0.5$ for Ψ = 60°.

The angle describing the orientation of maximum temperature zone (α), where the heat is locally concentrated, is measured for each Ψ. The results, illustrated in Fig. 18, indicate that by varying the mode mixity between 0° and 45°, the angle gradually decreases from 90° to 33°. However, the angle remains constant for Ψ greater than 45°. Further details of temperature distributions around the crack tip can be followed in Fig. 18.

In order to investigate the effect of loading rate on local phenomena around the crack tip, the angular temperature distribution on a specific circular path is illustrated for different mixed mode conditions (see Fig. 19). It should be noted that the path for determining the angular temperature distribution is assumed to be a circle, whose radius is equal to the distance from the crack tip to the point of occurrence of maximum temperature, as depicted by white circles in Fig. 18.

Results in Fig. 19 suggest that for the uncoupled problem, the temperatures of all points on the circular path are similar and equal to the reference temperature (T_0). However, as the loading rate increases, the trend of temperature distribution near the crack tip changes dramatically. Specifically, increasing the loading rate leads to more latent heat generation, resulting in generation of higher temperatures.

It should be noted that the latent heat produced by SMA (upper layer) is distributed into the lower layer due to the heat conductivity of

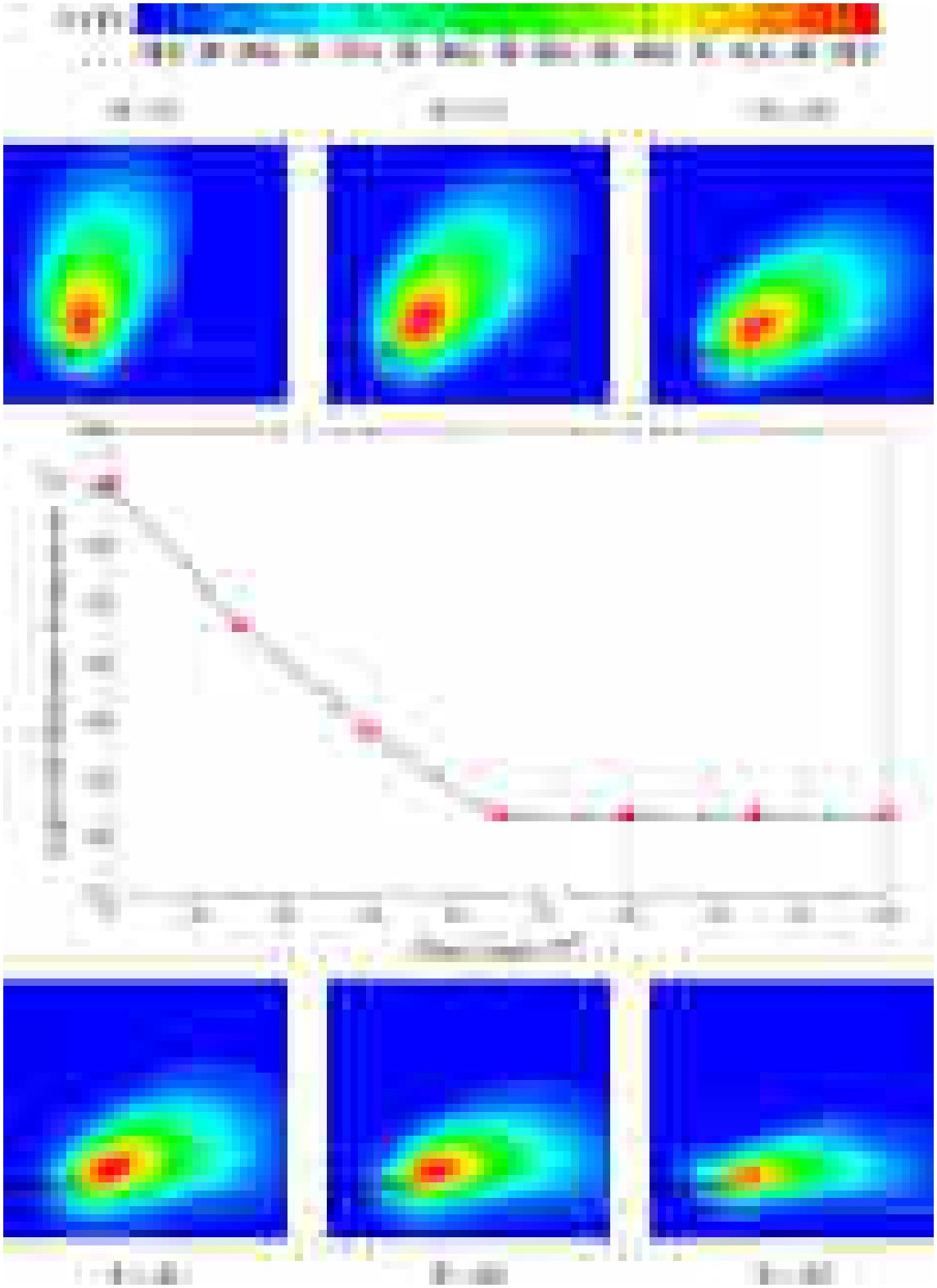

Fig. 18. Rotation of the temperature zone by varying the phase angles Ψ

elastoplastic material. This phenomenon is clearly observed in Fig. 19, in which the values of temperature, for angles below the zero degree, are greater than the ambient temperature.

Moreover, inspection of Fig. 19 indicates that the maximum temperature for $\Psi = 0^\circ$ appears in an angle close to 90°. The maximum temperature zone rotates to angles smaller than 90° by increasing the phase angle. For example, the maximum temperature occurs at angles 67° and 48° for $\Psi = 15^\circ$ and $\Psi = 30^\circ$, respectively. In addition, as mentioned before in Fig. 18, the orientation of maximum temperature zone (α) follows a decreasing trend for the phase angles below 45°($\Psi \leqslant 45^\circ$) while it remains constant for phase angles higher than 45° ($\Psi > 45^\circ$).

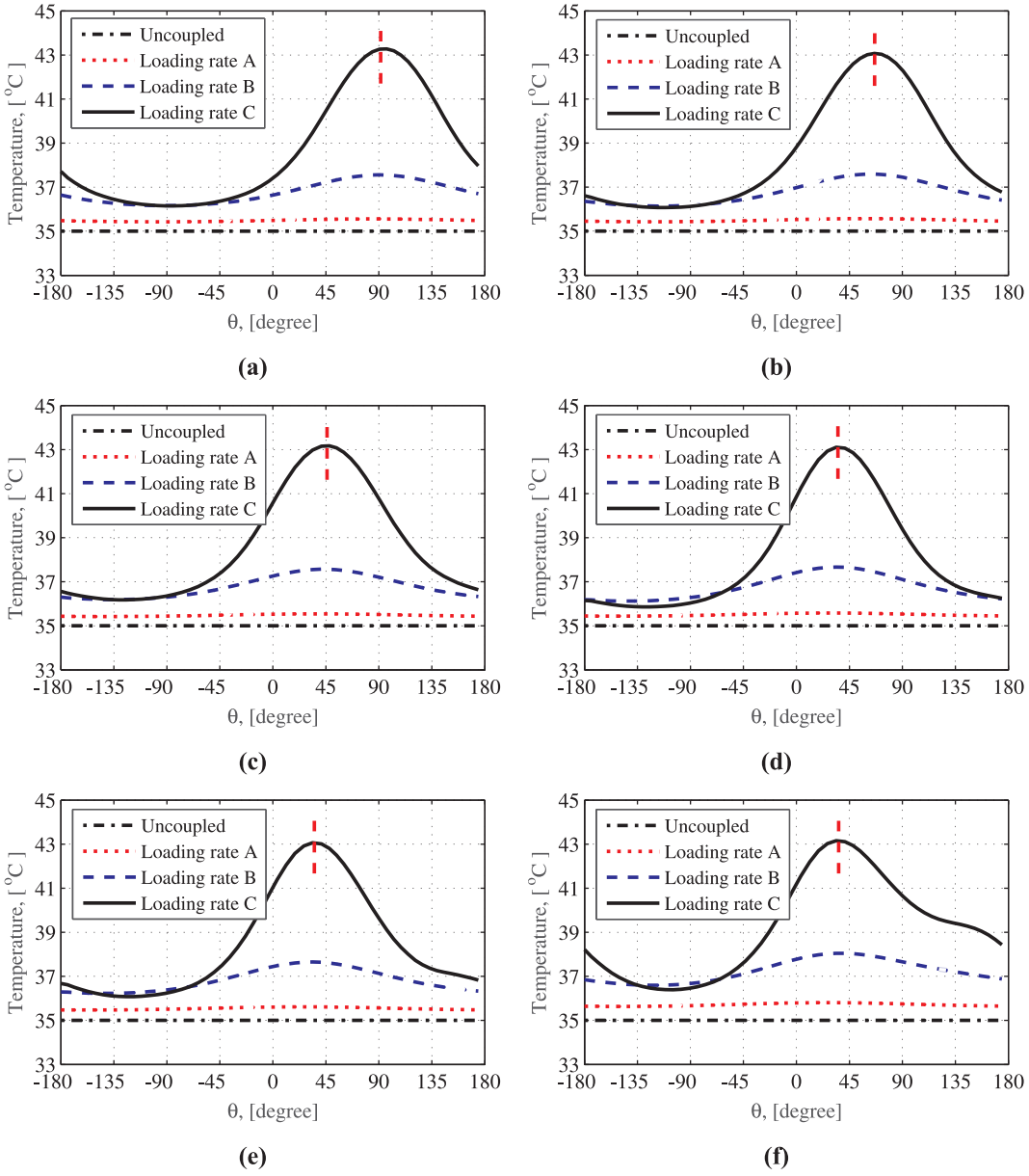

Fig. 19. Effect of applied loading rate on the angular temperature distribution for different phase angles (a) Ψ = 0°, (b) Ψ = 15°, (c) Ψ = 30°, (d) Ψ = 45°, (e) Ψ = 60°, (f) Ψ = 90°

8. Conclusion

Delamination analysis in layered composites consisting of shape memory alloy and elastoplastic layers is numerically addressed by considering the thermo-mechanical coupling model for SMA and the J_2 plasticity for elastoplastic material. Small-scale phase transformation and yielding zones are presumed. The path dependency of J-integral is investigated for a range of mixed-mode loading conditions, the Young's modulus of elastoplastic material, the hardening slope, the yield stress, the maximum transformation strain, and the loading rate. It is observed that for the hardening slope of 10 GPa, the mode mixity has a great effect on the energy release rate near the crack tip in such a way that even the trend of variations of energy release rate differs for different phase angles, whereas the results of the perfect plastic case are not influenced by changes of the phase angle. Moreover, it is shown that by increasing H, plasticity loses its effect on distribution of the energy release rate. As a result, for larger values of H, the trend of results for cracked SMA/elastoplastic composite becomes noticeably similar to homogenous cracked SMA material. In addition, an increase in energy release rate is observed by the increase of the initial yield stress (σ_{y0}) and the maximum transformation strain (ε^t_{max}). Moreover, it is illustrated that the generated latent heat in the crack tip induces a reduction in the energy release rate of coupled simulations. Finally, it can be concluded that while the temperature around the crack tip for the uncoupled problem remains equal to the reference temperature (T_0), the trend of temperature distribution near the crack tip dramatically changes as the loading rate increases.

Acknowledgement

The authors wish to acknowledge the technical support of the High Performance Computing Lab, School of Civil Engineering, University of Tehran. The financial support of Iran National Science Foundation (INSF) is gratefully acknowledged.

References

[1] Lagoudas DC, Shape. memory alloys: modeling and engineering applications. Springer Science & Business Media; 2008.
[2] Dolce M, Cardone D. Fatigue resistance of SMA-martensite bars subjected to flexural bending. Int J Mech Sci 2005;47(11):1693–717.
[3] Meng XL, Zheng YF, Cai W, Zhao LC. Two-way shape memory effect of a TiNiHf high temperature shape memory alloy. J Alloy Compd 2004;372(1):180–6.
[4] Wei ZG, Tang CY, Lee WB. Design and fabrication of intelligent composites based on shape memory alloys. J Mater Process Technol 1997;69(1):68–74.
[5] Shimamoto A, Ohkawara H, Nogata F. Enhancement of mechanical strength by shape memory effect in TiNi fiber-reinforced composites. Eng Fract Mech 2004;71(4):737–46.
[6] Fatemi Dehaghani P, Hatefi Ardakani S, Bayesteh H, Mohammadi S. 3D hierarchical multiscale analysis of heterogeneous SMA based materials. Int J Solids Struct 2017. 118–119: p. 24–40.
[7] Marfia S. Micro–macro analysis of shape memory alloy composites. Int J Solids Struct 2005;42(13):3677–99.
[8] Hu Z, Xiong K, Wang X. Study on interface failure of shape memory alloy (SMA) reinforced smart structure with damages. Acta Mech Sin 2005;21(3):286–93.
[9] Neuser S, Michaud V, White SR. Improving solvent-based self-healing materials through shape memory alloys. Polymer 2012;53(2):370–8.
[10] Ogisu T, Shimanuki M, Kiyoshima S, Takaki J, Takeda N. Damage suppression in CFRP laminates using embedded shape memory alloy foils. Adv Compos Mater 2004;13(1):27–42.
[11] Taketa I, Amano M, Kobayashi M, Ogisu T, Okabe Y, Takeda N. Modeling of thermo-mechanical behavior of Ti-Ni shape memory alloy foils embedded in carbon fiber reinforced plastic laminates. Adv Compos Mater 2005;14(1):25–42.
[12] Lagoudas D, Moorthy D, Qidwai M, Reddy J. Modeling of the thermomechanical response of active laminates with SMA strips using the layerwise finite element method. J Intell Mater Syst Struct 1997;8(6):476–88.
[13] Afshar A, Hatefi Ardakani S, Mohammadi S. Transient analysis of stationary interface cracks in orthotropic bi-materials using oscillatory crack tip enrichments. Compos Struct 2016;142:200–14.
[14] Afshar A, Hatefi Ardakani S, Mohammadi S, Stable. discontinuous space–time analysis of dynamic interface crack growth in orthotropic bi-materials using oscillatory crack tip enrichment functions. Int J Mech Sci 2018;140:557–80.
[15] Ashari SE, Mohammadi S. Delamination analysis of composites by new orthotropic bimaterial extended finite element method. Int J Numer Meth Eng 2011;86(13):1507–43.
[16] Belytschko T, Black T. Elastic crack growth in finite elements with minimal remeshing. Int J Numer Meth Eng 1999;45(5):601–20.
[17] Grogan D, Leen S, Brádaigh CÓJCS. An XFEM-based methodology for fatigue delamination and permeability of composites 2014;107:205–18.
[18] Huang Kai, Guo Licheng, Yu Hongjun. Investigation on mixed-mode dynamic stress intensity factors of an interface crack in bi-materials with an inclusion. Compos Struct 2018;202:491–9. https://doi.org/10.1016/j.compstruct.2018.02.078.
[19] Nagashima T, Omoto Y, Tani S. Stress intensity factor analysis of interface cracks using X-FEM. Int J Numer Meth Eng 2003;56(8):1151–73.
[20] Nasirmanesh A, Mohammadi S. XFEM buckling analysis of cracked composite plates. Compos Struct 2015;131:333–43.
[21] Yu T, Bui TQ, Liu P, Zhang C, Hirose S. Interfacial dynamic impermeable cracks analysis in dissimilar piezoelectric materials under coupled electromechanical loading with the extended finite element method. Int J Solids Struct 2015;67–68:205–18.
[22] Nguyen VP, Anitescu C, Bordas SP, Rabczuk T. Isogeometric analysis: an overview and computer implementation aspects. Math Comput Simul 2015;117:89–116.
[23] Nguyen VP, Kerfriden P, Bordas SP. Two-and three-dimensional isogeometric cohesive elements for composite delamination analysis. Compos B Eng 2014;60:193–212.
[24] Nguyen VP, Nguyen-Xuan H. High-order B-splines based finite elements for delamination analysis of laminated composites. Compos Struct 2013;102:261–75.
[25] Verhoosel CV, de Borst R. A phase-field model for cohesive fracture. Int J Numer Meth Eng 2013;96(1):43–62.
[26] Roy P, Deepu S, Pathrikar A, Roy D, Reddy J. Phase field based peridynamics damage model for delamination of composite structures. Compos Struct 2017;180:972–93.
[27] Wu J-Y, Nguyen VP, Nguyen CT, Sutula D, Bordas S, Sinaie S. *Phase field modeling of fracture.* Advances in. Applied Mechancis: Multi-scale Theory and Computation 2018;52.
[28] Sutula D, Kerfriden P, Van Dam T, Bordas SP. Minimum energy multiple crack propagation. Part I: Theory and state of the art review. Eng Fract Mech 2018;191:205–24.
[29] Sutula D, Kerfriden P, Van Dam T, Bordas SP. Minimum energy multiple crack propagation. Part-II: Discrete solution with XFEM. Eng Fract Mech 2018;191:225–56.
[30] Sutula D, Kerfriden P, Van Dam T, Bordas SP. Minimum energy multiple crack propagation. Part III: XFEM computer implementation and applications. Eng Fract Mech 2018;191:257–76.
[31] Menk A, Bordas SP. Numerically determined enrichment functions for the extended finite element method and applications to bi-material anisotropic fracture and polycrystals. Int J Numer Meth Eng 2010;83(7):805–28.
[32] Baxevanis T, Lagoudas D. A mode I fracture analysis of a center-cracked infinite shape memory alloy plate under plane stress. Int J Fract 2012;175(2):151–66.
[33] Birman V. On mode I fracture of shape memory alloy plates. Smart Mater Struct 1998;7(4):433.
[34] Gollerthan S, Herberg D, Baruj A, Eggeler G. Compact tension testing of martensitic/pseudoplastic NiTi shape memory alloys. Mater Sci Eng, A 2008;481–482:156–9.
[35] Gollerthan S, Young ML, Baruj A, Frenzel J, Schmahl WW, Eggeler G. Fracture mechanics and microstructure in NiTi shape memory alloys. Acta Mater 2009;57(4):1015–25.
[36] Gollerthan S, Young ML, Neuking K, Ramamurty U, Eggeler G. Direct physical evidence for the back-transformation of stress-induced martensite in the vicinity of cracks in pseudoelastic NiTi shape memory alloys. Acta Mater 2009;57(19):5892–7.
[37] Maletta C, Bruno L, Corigliano P, Crupi V, Guglielmino E. Crack-tip thermal and mechanical hysteresis in Shape Memory Alloys under fatigue loading. Mater Sci Eng, A 2014;616:281–7.
[38] Maletta C, Furgiuele F. Analytical modeling of stress-induced martensitic transformation in the crack tip region of nickel–titanium alloys. Acta Mater 2010;58(1):92–101.
[39] Maletta C, Sgambitterra E, Furgiuele F. Crack tip stress distribution and stress intensity factor in shape memory alloys. Fatigue Fract Eng Mater Struct 2013;36(9):903–12.
[40] Maletta C, Sgambitterra E, Niccoli F. Temperature dependent fracture properties of shape memory alloys: novel findings and a comprehensive model. Sci Rep 2016;6(1):17.
[41] Robertson SW, Mehta A, Pelton AR, Ritchie RO. Evolution of crack-tip transformation zones in superelastic Nitinol subjected to in situ fatigue: A fracture mechanics and synchrotron X-ray microdiffraction analysis. Acta Mater 2007;55(18):6198–207.
[42] Sgambitterra E, Maletta C, Furgiuele F. Investigation on Crack Tip Transformation in NiTi Alloys: Effect of the Temperature. Shape Memory and Superelasticity 2015;1(2):275–83.
[43] Yi S, Gao S. Fracture toughening mechanism of shape memory alloys due to martensite transformation. Int J Solids Struct 2000;37(38):5315–27.
[44] Stam G, van der Giessen E. Effect of reversible phase transformations on crack growth. Mech Mater 1995;21(1):51–71.
[45] Wang XM, Wang YF, Baruj A, Eggeler G, Yue ZF. On the formation of martensite in front of cracks in pseudoelastic shape memory alloys. Mater Sci Eng, A 2005;394(1):393–8.
[46] Freed Y, Banks-Sills L. Crack growth resistance of shape memory alloys by means of a cohesive zone model. J Mech Phys Solids 2007;55(10):2157–80.
[47] Jape S, Baxevanis T, Lagoudas D. On the fracture toughness and stable crack growth in shape memory alloy actuators in the presence of transformation-induced plasticity. Int J Fract 2018;209(1–2):117–30.
[48] Jape S, Baxevanis T, Lagoudas DC. Stable Crack Growth During Thermal Actuation of Shape Memory Alloys. Shape Memory and Superelasticity 2016;2(1):104–13.
[49] Hatefi Ardakani S, Afshar A, Mohammadi S. Numerical study of thermo-mechanical coupling effects on crack tip fields of mixed-mode fracture in pseudoelastic shape memory alloys. Int J Solids Struct 2016;81:160–78.
[50] Hatefi Ardakani S, Ahmadian H, Mohammadi S. Thermo-mechanically coupled fracture analysis of shape memory alloys using the extended finite element method. Smart Mater Struct 2015;24(4):045031.
[51] Freed Y, Banks-Sills L, Aboudi J. On the transformation toughening of a crack along an interface between a shape memory alloy and an isotropic medium. J Mech Phys Solids 2008;56(10):3003–20.
[52] Jin M, Bao ZB. Approximate SIF of Mode-I Crack Closure in Matrix by Knotted SMA Fiber. J Intell Mater Syst Struct 2009;20(10):1187–94.
[53] Chi Y, Li M, Xu L, Sun Q. Phase transition induced interfacial debonding in shape memory alloy fiber–matrix system. Int J Solids Struct 2015;75–76:199–210.
[54] Conte AL, Biffi CA, Tuissi A, Ali A. Computational Model for Delamination Growth at SMA-GFRP Interface of Hybrid Composite. Procedia Struct Integrity 2016;2:1538–45.
[55] Afshar A, Hatefi Ardakani S, Hashemi S, Mohammadi S. Numerical analysis of crack tip fields in interface fracture of SMA/elastic bi-materials. Int J Fract 2015;195(1–2):39–52.
[56] Belyaev S, Rubanik V, Resnina N, Rubanik Jr V, Demidova E, I.J.J.o.M.P.T. Lomakin. Bimetallic shape memory alloy composites produced by explosion welding: structure and martensitic transformation 2016;234:323–31.
[57] Belyaev S, Rubanik V, Resnina N, Rubanik Jr V, Rubanik O, Borisov VJPT. Martensitic transformation and physical properties of 'steel–TiNi'bimetal composite, produced by explosion welding 2010;83(4):276–83.
[58] Carka D, Landis CM. On the path-dependence of the J-integral near a stationary crack in an elastic-plastic material. J Appl Mech 2011;78(1):011006.
[59] Boyd JG, Lagoudas DC. A thermodynamical constitutive model for shape memory materials. Part I. The monolithic shape memory alloy. Int J Plast 1996;12(6):805–42.
[60] de Souza Neto EA, Peric D, Owen DR. Computational methods for plasticity: theory and applications. John Wiley & Sons; 2011.
[61] Ahmadian H, Hatefi Ardakani S, Mohammadi S. Strain-rate sensitivity of unstable localized phase transformation phenomenon in shape memory alloys using a non-local model. Int J Solids Struct 2015;63:167–83.
[62] Cho SB, Lee KR, Choy YS, Ryoji Y. Determination of stress intensity factors and boundary element analysis for interface cracks in dissimilar anisotropic materials. Eng Fract Mech 1992;43(4):603–14.
[63] Baxevanis T, Chemisky Y, Lagoudas DC. Finite element analysis of the plane strain crack-tip mechanical fields in pseudoelastic shape memory alloys. Smart Mater Struct 2012;21(9):094012.